

Resonant Biochemical Sensors Based on Photonic Bandgap Waveguides and Fibers

Maksim Skorobogatiy

Abstract I describe photonic bandgap (PBG) fiber-based resonant optical sensors of analyte's refractive index which have recently invoked strong interest due to the development of novel fiber types and of techniques for the activation of fiber microstructure with functional materials. Particularly, I consider two sensors types. One employs hollow-core photonic bandgap fibers where the core-guided mode is confined in the analyte's filled core through resonant effect in the surrounding periodic reflector. The other employs metallized photonic bandgap waveguides and fibers, where core-guided mode is phase-matched with a plasmon wave propagating at the fiber/analyte interface. In resonant sensors, one typically employs fibers with strongly nonuniform spectral transmission characteristics that are sensitive to changes in the real part of the analyte's refractive index. Moreover, if narrow absorption lines are present in the analyte transmission spectrum, due to Kramers–Kronig relation, this will also result in strong variation in the real part of the refractive index in the vicinity of an absorption line. Therefore, resonant sensors allow detection of minute changes both in the real part of the analyte's refractive index ($10^{-6} - 10^{-4}$ RIU) and in the imaginary part of the analyte's refractive index in the vicinity of absorption lines. Although the operational principle of almost all PBG fiber-based sensors relies on strong sensitivity of the PBG fiber losses to the value of the analyte's refractive index, particular transduction mechanisms for biodetection vary significantly. Finally, I detail various sensor implementations, modes of operation, as well as analysis of sensitivities for some of the common transduction mechanisms for biosensing applications.

Keywords Photonic bandgap fibers · Bragg fibers · Resonant optical sensors · Optical fiber sensors · Plasmonics · Plasmonic sensors

M. Skorobogatiy

Department of Engineering Physics, Ecole Polytechnique de Montréal, C.P. 6079, succ. Centre-ville, Montréal (Québec), Canada H3C 3A7

e-mail: yuji@ecei.tohoku.ac.jp

Contents

| | | |
|-----|--|----|
| 1 | Introduction | 45 |
| 2 | Detection Strategies for Absorption-Based Sensors | 47 |
| 3 | Sensing Using Hollow-Core Photonic Bandgap Fibers | 49 |
| 3.1 | Nonresonant Sensing | 50 |
| 3.2 | Resonant Sensing | 52 |
| 3.3 | Effect of Fiber Bending on Sensor Performance | 55 |
| 4 | Plasmon-Assisted Sensing Using PCFs | 56 |
| 4.1 | SPR Sensors Using Planar Photonic Bandgap Waveguides | 59 |
| 4.2 | SPR Sensors Using Photonic Bandgap Bragg Fibers | 62 |
| 4.3 | SPR Sensors Using Photonic Bandgap Honeycomb Fibers | 65 |
| 5 | Concluding Remarks | 69 |
| | References | 69 |

Abbreviations

| | |
|-----|---------------------------|
| FOS | Fiber-optic sensors |
| PBG | Photonic band gap |
| PCF | Photonic crystal fiber |
| PCR | Polymerize chain reaction |
| SPR | Surface plasmon resonance |
| TIR | Total internal reflection |

Symbols

| | |
|-------------------|--|
| d | Layer thickness in a multilayer waveguide |
| dA | Area differential in the transverse cross section of a waveguide |
| E | Electric field vector |
| E_t | Transverse electric field vector |
| f | Overlap factor |
| H | Magnetic field vector |
| H_t | Transverse magnetic field vector |
| L | Waveguide length |
| n | Refractive index |
| P | Power of guided light |
| R_{core} | Fiber core diameter |
| R_{bend} | Fiber bending radius |
| S_a | Amplitude sensitivity |
| S_λ | Spectral sensitivity |
| \hat{z} | Vector along the waveguide direction |
| α | Waveguide loss coefficient per unit of length |
| ε | Relative permittivity |
| λ | Wavelength of light in vacuum |
| δ | Small parameter characterizing changes in the measurand |

1 Introduction

Research and development into fiber-optic sensors (FOS) for biological and chemical sensing has made a lot of progress during the last 10 years. This is due to the appealing properties of FOS, such as immunity to electromagnetic interference, safety in explosive environments, and potential to provide continuous quantitative and qualitative real-time analysis. Chemically sensitive thin films deposited on selected areas of optical fibers can influence the propagation of light in such fibers, depending on the presence or absence of chemical molecules in the surrounding environment [38]. A wide range of optical sensors has been developed for selective biomolecule detection. Most of them have reliability issues as they employ very fragile antibodies as sensing elements. These sensors include high refractive index waveguides [30], SPR sensors [5], resonant mirrors [62], and classical fiber-optical sensors [11, 47]. Most optical sensors are based on evanescent wave sensing, where the perturbations in the refractive index close to the sensor surface are probed by the exponentially decaying optical wave. Such sensors have proven to be highly sensitive in detection of small targets such as proteins and viruses, but they experience difficulties in detecting larger targets such as bacteria (0.5–5 μm), since in that case much larger penetration of the evanescent field into analyte is required [66, 67].

PCFs and photonic bandgap (PBG) fibers (which are a subset of PCFs) promise a viable technology for the mass production of highly integrated and intelligent sensors in a single manufacturing step. In standard TIR fiber-based evanescent-wave sensors, the fiber polymer jacket is stripped and the fiber cladding is polished to the core in order to obtain an overlap between the optical field and analyte, with sensor sensitivity proportional to such an overlap. Compared to the conventional solid-core optical fibers, PCFs offer a number of unique advantages in sensing applications. A defining feature of a microstructured fiber is the presence of air holes running along its entire length. Fiber-optical properties are then determined by the size, shape, and relative position of the holes. Particularly, a remarkable ability of PCFs is to accommodate biological and chemical samples in gaseous or liquid forms inside of the air holes in the immediate vicinity of the fiber core [14, 15, 32]. The concept of combining optical detection with PCF devices is appealing as it achieves dual use of the PCF as light guiding and as a fluidic channel. The PCF's architecture makes it a very promising sensing platform for chemical and biological detection. First, PCFs naturally integrate optical detection with the microfluidics, allowing for continuous on-line monitoring of dangerous samples in real time without exposing the personnel to danger. In addition, the samples can be transferred in the enclosed PCF optofluidic system for further confirmation analysis, e.g., polymerase chain reactions (PCR), if needed. Such channels can be further functionalized with biorecognition layers that can bind and progressively accumulate target biomolecules, thus enhancing sensor sensitivity and specificity. Second, the PCF hole size is in sub-100 μm range, leading to very small fluid samples required for sensing. Third, PCF-based sensors can be

coiled into very long sensing cells (~ 10 m), thus dramatically increasing their sensitivity. The same is impossible to achieve with traditional TIR fiber sensors as side-polishing step limits sensor length to several centimeters. Fourth, the desired PCFs can be mass-produced using commercial fiber draw tower in a very cost-effective manner. Fifth, the PCFs can potentially be scaled up into a two-dimensional array with small dimensions, which is suitable for making portable point-of-care devices for simultaneous on-site detection of different kinds of analytes. Sixth, PCFs can be designed to guide light directly in their analyte-field hollow cores [44]. In such fibers, light-analyte coupling is considerably stronger than that in evanescent sensors.

In this chapter, I describe PBG fiber-based resonant optical sensors, which have recently invoked strong interest due to development of novel fiber types and of techniques for activation of the fiber microstructure with functional materials. In resonant sensors, one typically employs fibers with strongly non-uniform spectral transmission characteristics that are sensitive to changes in the real part of the analyte's refractive index. Moreover, if narrow absorption lines are present in the analyte's transmission spectrum, due to Kramers–Kronig relation, this will also result in strong variation in the real part of the refractive index in the vicinity of an absorption line. Therefore, resonant sensors allow detection of minute changes both in the real part of the analyte's refractive index and in the imaginary part of the analyte's refractive index in the vicinity of absorption lines. Although the operational principle of almost all PBG fiber-based sensors relies on strong sensitivity of the PBG fiber losses to the value of the analyte's refractive index, particular transduction mechanism for biodetection can vary. Thus, in one implementation, one can label the target biomolecules with highly absorbing particles of known absorption spectra, such as metal nanoparticles or quantum dots. The presence of such particles in the aqueous fiber core can then be quantified by detecting the appearance of the absorption lines in the fiber transmission spectrum, or through resonant changes in the fiber transmission losses induced by variations in the real part of the core refractive index. In another implementation, a functional layer that binds specific biomolecules can be deposited on the inside of the hollow fiber core. Biomolecule binding events to such a layer can then be detected through resonant changes in the fiber transmission losses induced by variations in the real part of the layer refractive index.

In this chapter, I discuss two types of resonant sensors. One type of sensor relies on changes in the optical confinement of a mode propagating inside of a resonant fiber structure due to changes in the real part of an analyte's refractive index. An example of such a resonant sensor is a photonic bandgap fiber featuring a hollow core filled with analyte. The geometry of such a fiber is chosen to provide strong optical confinement of the guided mode in the analyte's filled core for a particular value of an analyte's refractive index. When changing the real part of an analyte's refractive index, resonant condition for mode confinement will change, resulting in strong variation of the fiber transmission loss (see Fig. 1a, top left). Such sensors can also be used in a standard non-resonant mode for detection of changes in the imaginary part of the analyte's refractive index (analyte absorption) (see Fig. 1a bottom left). Even in non-resonant mode, sensitivity of the hollow-core PBG

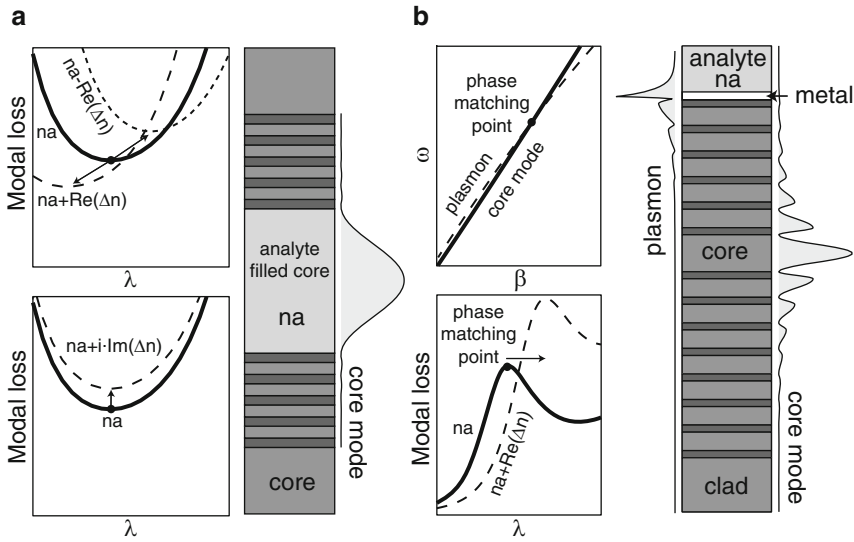


Fig. 1 Operational principles and schematics of two types of the resonant optical sensors. (a) Analyte-filled hollow photonic bandgap fiber-based sensor. Transmission loss through such a sensor is very sensitive to the values of both the real and imaginary parts of the analyte's refractive index. (b) Sensor operating near the phase-matching point of a convenient-to-excite core-guided mode and a second mode featuring large overlap with the analyte region. In the case of phase-matching with a plasmon mode, propagation loss of a core-guided mode is strongly dependent on the real part of the analyte's refractive index

fiber-based sensors is, generally, superior to that of traditional TIR fiber-based sensors due to greatly improved modal overlap with analyte. The second type sensor considered in this chapter is operated in the vicinity of a phase-matching wavelength between an easy to excite core-guided mode and some other mode that shows high sensitivity of its propagation properties to changes in the real part of the analyte's refractive index (Fig. 1b). For example, by activating fiber surface with a thin metal layer, at a specific resonant wavelength, one can induce strong optical loss of a core-guided mode due to coupling to an absorbing plasmon mode propagating at the metal/analyte interface. As plasmon mode is largely delocalized in the analyte region, wavelength of phase-matching between the two modes will be very sensitive to the value of the real part of analyte's refractive index.

2 Detection Strategies for Absorption-Based Sensors

I now describe amplitude-based and spectral-based detection strategies for sensors that exploit changes in their transmission losses in the presence of a target analyte.

In the amplitude-based detection methodology, one operates at a fixed wavelength λ and records changes in the amplitude of a signal, which are then reinterpreted in terms of changes in the analyte's refractive index. To characterize

sensitivity of a fiber-based sensor of length L , one employs an amplitude sensitivity function $S_a(\lambda, L)$, which is defined as a relative change in the intensity $P(\delta, \lambda, L)$ of a transmitted light for small changes in the measurand δ . Note that δ can be any parameter that influences transmission properties of a fiber sensor. This includes concentration of absorbing particles in the analyte, thickness of a biolayer that can change due to capture of specific biomolecules, as well as real or imaginary parts of the analyte's refractive index. Amplitude sensitivity is thus defined as:

$$S_a(\lambda, L) = \lim_{\delta \rightarrow 0} \frac{P(\delta, \lambda, L) - P(0, \lambda, L)}{\delta \cdot P(0, \lambda, L)} = \frac{\partial P(\delta, \lambda, L) / \partial \delta |_{\delta=0}}{P(0, \lambda, L)}. \quad (1)$$

Denoting by $\alpha(\delta, \lambda)$, the fiber propagation loss at a fixed value δ of a measurand, light intensity at the fiber output can be written as:

$$P(\delta, \lambda, L) = P_{\text{in}}(\lambda) \exp(-\alpha(\delta, \lambda)L), \quad (2)$$

where $P_{\text{in}}(\lambda)$ is the light intensity launched into a fiber. Substituting (2) into (1), the amplitude sensitivity function can be then expressed as:

$$S_a(\lambda, L) = -\partial \alpha(\delta, \lambda) / \partial \delta |_{\delta=0} \cdot L, \quad (3)$$

As follows from (3), sensor sensitivity is proportional to the sensor length L . In turn, as follows from (2), the maximal sensor length is limited by the absorption loss of a fiber. Defining $P_{\text{det}}(\lambda)$ to be the power detection limit at which changes in the light intensity can still be detected reliably, the maximal sensor length allowed by the power detection limit can be calculated from (2) as:

$$L = \frac{\log(P_{\text{in}}(\lambda) / P_{\text{det}}(\lambda))}{\alpha(0, \lambda)}. \quad (4)$$

Defining a new function $\eta_{\text{det}}(\lambda) = \log(P_{\text{in}}(\lambda) / P_{\text{det}}(\lambda))$, maximal sensitivity allowed by the power detection limit can be written using (3) as:

$$S_a(\lambda) = -\eta_{\text{det}}(\lambda) \frac{\partial \alpha(\delta, \lambda) / \partial \delta |_{\delta=0}}{\alpha(0, \lambda)}. \quad (5)$$

In all the simulations that follow, I assume that $\eta_{\text{det}}(\lambda) = 1$, which allows us to characterize an inherent sensitivity of a sensor system, while separating it from the issue of a power budget that might bring additional sensitivity enhancement. Finally, given sensor amplitude sensitivity, to estimate sensor resolution of a measurand δ , one can use expression (1). Assuming that the minimal detectable relative change in the signal amplitude is $(\Delta P / P)_{\text{min}}$ (which is typically on the order of 1% if no advanced electronics is used), then the minimum value of a measurand that can be detected by such a sensor is:

$$\delta_{\text{min}} = \frac{(\Delta P / P)_{\text{min}}}{S_a(\lambda)}. \quad (6)$$

Another popular sensing methodology is based on spectral interrogation. It uses detection of displacements of spectral singularities in the presence of a measurand with respect to their positions for a zero measurand. This sensing approach is particularly effective in the resonant sensor configurations that feature sharp transmission or absorption peaks in their spectra. Defining $\lambda_p(\delta)$ to be the position of a peak in a sensor transmission spectrum as a function of a measurand value δ , spectral sensitivity function can be defined as:

$$S_\lambda = \partial\lambda(\delta)/\partial\delta|_{\delta=0}. \quad (7)$$

Given sensor spectral sensitivity, to estimate sensor resolution of a measurand δ , one can use expression (7). Thus, assuming that the minimal detectable spectral shift in the peak position is $(\Delta\lambda_p)_{\min}$ (which is typically on the order of 0.1 nm in the visible spectral range if no advanced optical detection is used), then the minimum value of a measurand that can be detected by such a sensor is:

$$\delta_{\min} = \frac{(\Delta\lambda_p)_{\min}}{S_\lambda}. \quad (8)$$

3 Sensing Using Hollow-Core Photonic Bandgap Fibers

Recently, novel type of optical fibers, called hollow-core PBG fibers, has been introduced. In their cross section, PBG fibers can contain periodically arranged micron-sized air voids [31, 46, 53] (Fig. 2a), rings of holes separated by nanosupports [4, 61] (Fig. 2b), or a periodic sequence of micron-sized layers of different materials [45, 57] (Fig. 2c). PBG fibers are currently available in silica glass, polymer, and specialty soft glass implementations. The key functionality of such

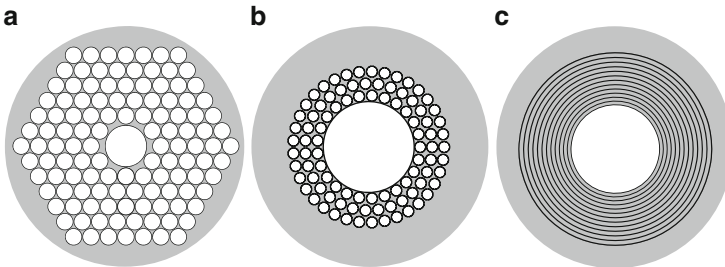


Fig. 2 Various types of hollow-core photonic bandgap fibers. (a) Photonic crystal fiber featuring small hollow core surrounded by a periodic array of large air holes. (b) Microstructured fiber featuring medium-sized hollow core surrounded by several rings of small air holes separated by nano-size bridges. (c) Bragg fiber featuring large hollow core surrounded by a periodic sequence of high and low refractive index layers

fibers is their ability to guide light directly in the hollow or liquid-filled cores with refractive index smaller than that of a surrounding cladding material. Unlike microstructured fibers, PBG fibers confine light in their hollow cores by photonic bandgap effect, rather than by TIR. Practically, bandgaps are defined as frequency regions of enhanced fiber transmission, and they are the result of destructive interference of the core-guided light inside of the fiber microstructured cladding. When launching spectrally broad light into a PBG fiber, only the spectral components guided by the fiber bandgaps will reach the fiber end, while all the spectral components not located within the bandgaps will be irradiated out near the fiber coupling end. Moreover, even in the absence of fiber material losses, core-guided modes always exhibit radiation loss. This is a direct consequence of guidance in a core with refractive index smaller than that of a cladding. As we will see in what follows, core mode radiation loss can be very sensitive to the value of the real part of the refractive index of the material filling the fiber core, which can be utilized for sensor applications. Finally, PBG fibers have a tendency to improve the beam quality of guided light, while being effectively single mode in the limit of long propagation distances. This is a consequence of the fact that radiation losses (and, generally, absorption losses too) of the core-guided modes of a PBG fiber are strongly differentiated with only a few low-order modes having small propagation losses. Thus, when exciting several modes at the fiber input end, only the modes having the lowest losses will survive till the fiber end. For historical reference, I mention that before the invention of the all-dielectric PBG fibers, guidance in the hollow-core fibers has been demonstrated in the context of metal coated capillaries [22, 49].

I now detail some of the advantages offered by the hollow-core PBG fibers for sensing applications. One has to distinguish two modes of operation of such sensors. First, is sensing of changes in the imaginary part of the analyte's refractive index (analyte absorption) by detecting the presence and strength of the narrow absorption bands in the fiber transmission spectrum. This is the simplest, non-resonant application of the hollow PBG fibers for optical sensing in which one only takes advantage of the large optical field overlap with analyte. In such sensors, signal strength due to analyte absorption, as well as sensor sensitivity are directly proportional to the sensor length. Recently, several experimental implementations of such absorption-based sensors have been demonstrated [7, 8, 28, 33, 54]. Second mode of operation of a PBG fiber-based sensor is sensing of changes in the real part of the analyte's refractive index by detection of shifts in the fiber bandgap position. As it will be explained in the following sections, such a sensor operates in the resonant regime with sensitivity that is largely independent of the sensor length.

3.1 *Nonresonant Sensing*

Classic perturbation theory considerations [55] predicts that changes in the effective refractive index of a guided mode Δn_{eff} are related to the changes in the

refractive index Δn_a of analyte infiltrating the fiber, through the overlap factor f defined as:

$$\Delta n_{\text{eff}} = \Delta n_a \cdot f = \text{Re}(\Delta n_a) \cdot f + i \cdot \text{Im}(\Delta n_a) \cdot f$$

$$f = \frac{\int_{\text{analyte}} dA |\mathbf{E}|^2}{\text{Re} \left(\hat{\mathbf{z}} \cdot \int_{\text{crosssection}} dA \mathbf{E}_t^* \times \mathbf{H}_t \right)}, \quad (9)$$

where \mathbf{E}_t , and \mathbf{H}_t are the transverse electromagnetic fields of a fiber mode, while \mathbf{E} is a complete electric field of a mode. Strictly speaking, expression (9) is only valid for the truly guided square integrable modes of the TIR fibers. In the case of hollow-core PBG fibers, the guided modes are, generally, non-square integrable leaky modes [16]. In this case, however, expression (9) can still be used but only approximatively. Particularly, to avoid divergence in the denominator of (9), one performs integration only over the finite fiber cross section limited by the interface between the multilayer reflector and a cladding. For the hollow-core PBG fibers, detailed simulations show that f is typically larger than 0.9. The value of an overlap increases rapidly when the fiber core size increases, reaching values higher than 0.99 for even the small core sizes $R_{\text{core}} \sim 5 - 10\lambda$ (compared to the wavelength of light). Such a high value of the overlap factor is explained by high confinement of the guided mode in the fiber core (see, for example, energy flux distribution of the core-guided mode in Fig. 1a right).

Expression (9) is fundamental for the analysis of non-resonant absorption-based sensors. Consider, for example, a microstructured or a hollow-core fiber filled with aqueous solution. One possible biosensor implementation utilizing such fibers can, for example, monitor presence and concentration of specific biomolecules labeled by highly absorbing nanoparticles. In such a sensor, biomolecules in the aqueous solution are purged through the fiber microstructure. Defining C to be the concentration (measurand; $\delta = C$ in (1)) of the absorbing particles mixed with analyte, and assuming that nanoparticle bulk absorption per unit of concentration is $\alpha_C(\lambda)$, while fiber loss in the absence of nanoparticles is $\alpha_f(\lambda)$, then total fiber loss in the presence of absorbing nanoparticles can be written using (9) as:

$$\alpha(C, \lambda) = \alpha_f(\lambda) + f C \alpha_C(\lambda). \quad (10)$$

In the derivation of (10), I used the fact that $\text{Im}(\Delta n_a) \sim C \alpha_C$, $\alpha(C, \lambda) \sim \text{Im}(n_{\text{eff}})$. By substituting (10) into (5), I now find expression for the maximal non-resonant sensor sensitivity to changes in the nanoparticle concentration:

$$S_a(\lambda) = -f \frac{\alpha_C(\lambda)}{\alpha_f(\lambda)}. \quad (11)$$

Note that as nanoparticle absorption $\alpha_C(\lambda)$ is completely independent from the fiber loss $\alpha_f(\lambda)$ in the absence of nanoparticles, sensitivity (11) of a non-resonant

sensor is, thus, directly proportional to the fiber length $L \sim 1/\alpha_f(\lambda)$. Consequently, to increase sensor sensitivity, one has to simply work with longer fibers featuring low propagation loss.

3.2 Resonant Sensing

Note that expression (9), when applied to PBG fibers, does not account for the spectral shift of the PBG fiber bandgap (see Fig. 1a top left) due to changes in the real part of the refractive index of an analyte. In fact, for the hollow-core PBG fibers in place of (9), one has to use the following modified expression:

$$\Delta n_{\text{eff}} = \text{Re}(\Delta n_a) \cdot f + i[\text{Im}(\Delta n_a) \cdot f + \text{Re}(\Delta n_a) \cdot f_{\text{rad}}]. \quad (12)$$

Here, f_{rad} is a radiation factor that describes changes in the confinement losses of a photonic bandgap-guided mode due to spectral shift of a fiber bandgap caused by changes in the real part of the refractive index of an analyte.

To understand the radiation loss contribution in (12), one has to recall the principles of design and operation of the hollow-core PBG fibers. Consider, as an example, the case of a hollow-core plastic Bragg fiber featuring a water-filled core (refractive index n_w) surrounded by a Bragg reflector (Fig. 3a) made of a periodic sequence of two optically different materials with refractive indices n_l, n_h , which are assumed to be purely real [44, 45, 50]. I now design Bragg reflector to feature the fundamental bandgap in the visible at $\lambda_0 = 0.5\mu\text{m}$. The reflector layer thicknesses d_l, d_h have to be chosen in a very specific way as to guarantee the destructive interference of guided light in the periodic fiber cladding, hence efficient modal confinement in the fiber hollow core. Particularly, by choosing the reflector layer thicknesses to satisfy the quarter wave condition:

$$d_{l,h} = \frac{\lambda_0}{4\sqrt{n_{l,h}^2 - \text{Re}(n_{\text{core}})^2}}. \quad (13)$$

One guarantees that the fundamental bandgap of a Bragg reflector is centered in the near vicinity of a design wavelength λ_0 [16].

I now consider particular implementation of a Bragg fiber having the core of radius $R_{\text{core}} = 25 \mu\text{m}$ surrounded by six reflector layers with $n_h = 1.6, n_l = 1.4$ and the layer thicknesses given by (13), where $n_{\text{core}} = 1.34$. In Fig. 2b in thick solid curve I present propagation loss of the fundamental Gaussian-like HE_{11} core mode of a Bragg fiber. In fact, HE_{11} mode plays a key role in the operation of a majority of the hollow-core-based sensors as it is the easiest mode to excite with an external Gaussian-like laser source. While total propagation loss is a sum of the modal radiation and absorption losses, this particular fiber is operating in the radiation

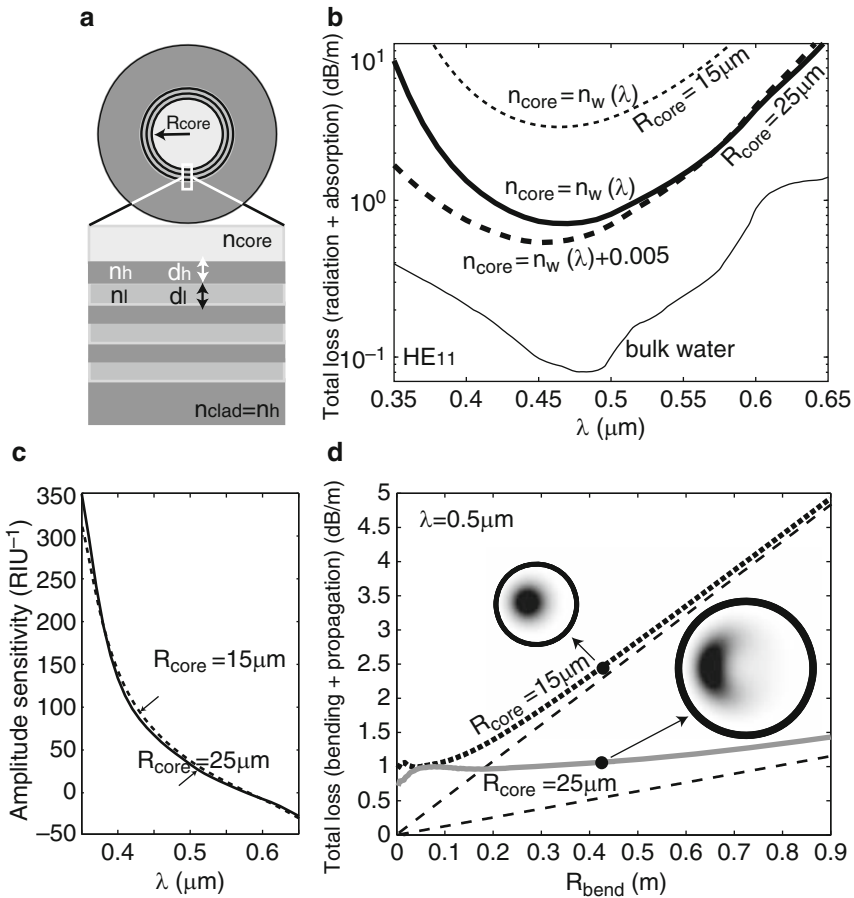


Fig. 3 Refractive index sensors based on hollow-core PBG Bragg fibers. (a) Schematic of a hollow-core Bragg fiber filled with aqueous analyte of refractive index $n_w(\lambda)$. (b) Radiation dominated propagation loss of a core-guided HE_{11} mode for two Bragg fibers with core radii $R_{core} = 25 \mu\text{m}$ (solid curve) and $R_{core} = 15 \mu\text{m}$ (thin dashed curve). When analyte’s refractive index changes, so does the radiation loss of a fiber-core mode (thick dashed curve). For the reference, in thin solid line, I present absorption loss of an aqueous analyte in the visible. (c) Amplitude sensitivity of the analyte filled Bragg fiber-based sensor for two radii of the fiber core. Note that maximal sensitivity is almost independent of the fiber-core radius. (d) Effect of macro-bending on sensor performance, comparison of two Bragg fibers with different core radii. In solid lines, I present total loss (bending + propagation) of a HE_{11} mode as a function of fiber bending radius. For comparison, losses of straight fibers of comparable lengths are presented as dashed lines. Fibers of smaller-core size exhibit stronger propagation losses; however, for the same value of the fiber bending radius, beam quality in smaller-core fibers is greatly superior to that in larger-core fibers

dominated regime; for comparison, bulk absorption loss of water is presented in Fig. 3b in thin solid line. Note that modal propagation loss reaches its minimum at the center of a photonic bandgap at $\sim 0.46 \mu\text{m}$, while increasing rapidly towards

the edges of a bandgap. When changing the real part of the refractive index of an analyte filling the fiber core, resonant condition (13) is no longer satisfied, thus leading to spectral displacement of the fiber bandgap (see dashed lines in Fig. 3b). Therefore, even for small changes in the analyte's refractive index, due to spectral shift in the position of a reflector bandgap, fiber propagation loss can vary substantially. Moreover, due to resonant nature of bandgap guiding, bandgap shift due to changes in the real part of the analyte's refractive index can have a substantially stronger effect on the propagation losses of a core-guided mode than changes in the absorption coefficient of an analyte. Particularly, in (13) one can calculate that at the operational wavelength of $0.5 \mu\text{m}$, $f \simeq 1$, while $f_{\text{rad}} \simeq 2.4 \times 10^{-4}$. Therefore, change of 1 dB/m loss in the analyte absorption coefficient ($\text{Im}(\Delta n_a) \simeq 0.9 \times 10^{-8}$), or change of $\text{Re}(\Delta n_a) \simeq 3.8 \times 10^{-5}$ in the real part of the analyte's refractive index, result in the same 1 dB/m change in the modal propagation loss.

I now investigate amplitude and spectral sensitivities of the hollow-core PBG fiber-based sensors. In Fig. 3c I present amplitude sensitivity (5) of a Bragg fiber-based sensor to changes in the real part of the analyte's refractive index $\delta = \text{Re}(\Delta n_a)$. Note that sensitivity varies strongly as a function of the wavelength of operation, increasing rapidly towards the bandgap edges. Inside of a bandgap and in the vicinity of a design wavelength, amplitude sensitivity is on the order of $S_a \sim 100 \text{ RIU}^{-1}$. Assuming that 1% of change in the amplitude of a transmitted light can be detected reliably, this results in sensor resolution of $\text{Re}(\Delta n_a)_{\text{min}} \sim 10^{-4} \text{ RIU}$. Finally, in the vicinity of a bandgap center at 470 nm the total fiber loss is $\sim 0.7 \text{ dB/m}$, thus defining sensor length to be on the order of $\sim 6 \text{ m}$.

In a similar fashion, spectral sensitivity can be defined using (7) by detecting spectral shift in the bandgap center (wavelength of the fiber lowest loss) resulting in a spectral sensitivity $S_\lambda \sim 5, 300 \text{ nm/RIU}$. Assuming that 0.1 nm spectral shift in the position of a bandgap center can be detected reliably, this results in the sensor resolution of $\text{Re}(\Delta n_a)_{\text{min}} \sim 2 \times 10^{-5} \text{ RIU}$, which is comparable to the resolution achieved by the amplitude method.

Interestingly, maximal sensitivity of a resonant hollow-core PBG fiber sensor does not depend strongly on the fiber length. To demonstrate that, in Fig. 3b, I also present losses of an HE_{11} mode of a hollow-core Bragg fiber, with a core radius $R_{\text{core}} = 15 \mu\text{m}$ and otherwise identical parameters to the Bragg fiber with $R_{\text{core}} = 25 \mu\text{m}$. Note that losses of a smaller-core fiber are almost ten times as high as losses of a larger-core fiber. This signifies that the maximal allowed length of a sensor based on a smaller-core fiber is almost ten times shorter than the length of a sensor based on a larger-core fiber. In Fig. 3c, I also plot the maximal sensitivity (5) of a Bragg fiber-based sensor with a core radius $R_{\text{core}} = 15 \mu\text{m}$ and note that it is almost identical to that of a larger-core fiber. This interesting, while somewhat counterintuitive, result is a direct consequence of the fact that in PBG fibers operating in the radiation dominated regime, fiber propagation loss and radiation factor are not independent parameters. Particularly, starting from (12), and assuming that the fiber loss for a neutral analyte is $\alpha_f(\lambda)$, then PBG fiber

absorption loss $\alpha(\Delta n_a, \lambda)$ in the presence of changes in the real part of the analyte's refractive index is described by:

$$\alpha(\Delta n_a, \lambda) = \alpha_f(\lambda) + \frac{4\pi}{\lambda} \text{Re}(\Delta n_a) \cdot f_{\text{rad}}. \quad (14)$$

In the case of Bragg fibers operating in the radiation dominated regime, one generally finds that $f_{\text{rad}} \sim \alpha_f(\lambda)$. Therefore, maximal amplitude sensitivity as defined by (5) will not depend on the fiber loss, and as a consequence, it will not depend on the sensor length. This finding promises a significant advantage of PBG fiber-based resonant sensors compared to their conventional absorption-based counterparts. Particularly, compact and highly sensitive sensors that utilize short PBG fiber pieces and that do not require fiber coiling are more convenient to use, and easier to maintain than their conventional counterparts that utilize long coiled fibers.

3.3 Effect of Fiber Bending on Sensor Performance

I finally comment on the effects of fiber core size and fiber bending on the performance of a hollow-core PBG fiber-based sensor. In fact, the value of a core radius R_{core} influences strongly modal guiding in such fibers. Particularly, core mode propagation losses in a straight fiber decrease rapidly with increase in the hollow core size (typically $\sim R_{\text{core}}^{-3}$), thus allowing, in principle, longer sensor lengths and higher sensitivities (for non-resonant sensing) when using fibers with larger cores. At the same time, mixing of the fundamental core mode with higher-order high-loss modes increases dramatically with increase in the hollow core size. This also results in the degradation of the quality of a guided beam and, potentially, resulting in reduced overlap with analyte. Therefore, while designing hollow-core PBG fiber-based sensors, one has to be aware of the tradeoff between longer sensor lengths versus bending induced beam degradation. As an example, in Fig. 3d, I compare bending losses and beam profiles of the two Bragg fibers having core radii $R_{\text{core}} = 15 \mu\text{m}$ and $R_{\text{core}} = 25 \mu\text{m}$ and featuring the same Bragg reflector as described above. All the simulations are performed at $\lambda = 0.5 \mu\text{m}$. In Fig. 3d, in thick solid lines, I plot total losses of a 90° bend as a function of the bending radius, while in dashed lines, I present, for the sake of comparison, propagation losses of straight fibers of equivalent lengths. Simulations show that in the bending loss dominated regime (fiber bending radius is small), bending loss depends weakly on the fiber core size. However, for larger bending radii, propagation loss is largely determined by the loss of the fundamental core mode of a straight fiber, which increases rapidly when core size decreases. Moreover, for the same value of bending radius, intensity distribution inside of a fiber featuring larger core shows strong mode mixing and pronounced beam profile degradation, while field intensity

distribution in a smaller-core fiber resembles that of a fundamental core mode (see also Fig. 1b).

4 Plasmon-Assisted Sensing Using PCFs

In this section, I describe another type of a resonant sensor operating in the vicinity of a phase-matching point between an easy-to-excite core-guided mode of a waveguide (fiber) with another mode that has strong overlap with analyte region (see Fig. 1b). In the particular case described in what follows, the mode that has strong overlap with analyte is a highly lossy plasmon wave.

Propagating at the metal/dielectric interface, surface plasmons [1] are extremely sensitive to changes in the refractive index of the dielectric. This feature constitutes the core of many SPR sensors. Typically, these sensors are implemented in the Kretschmann–Raether prism geometry where p-polarized light is launched through a glass prism and reflected from a thin metal (Au, Ag) film deposited on the prism facet [34]. The presence of a prism allows phase-matching of an incident electromagnetic wave with a plasmonic wave at the metal/ambient dielectric interface at a specific combination of the angle of incidence and wavelength. Mathematically, phase-matching condition is expressed as an equality between the plasmon wavevector and a projection of the wavevector of an incident wave along the interface. Since plasmon excitation condition depends resonantly on the value of the refractive index of an ambient medium within 100–300 nm from the interface, the method enables, for example, detection, with unprecedented sensitivity, of biological binding events on the metal surface [37]. The course of a biological reaction can then be followed by monitoring angular [37, 39], spectral [65] or phase [20, 29] characteristics of the reflected light. However, the high cost and large size of commercially available systems makes them useful mostly in a laboratory, while many important field and other applications still remain out of the reach for this method.

The use of optical waveguides and fibers instead of bulk prism configuration in plasmonic sensors offers miniaturization, high degree of integration, and remote-sensing capabilities. In fiber and waveguide-based sensors, one launches the light into a waveguide core and then uses coupling of a guided mode with a plasmon mode to probe for the changes in the ambient environment. To excite efficiently a surface plasmon, the phase-matching condition between a plasmon and a waveguide mode has to be satisfied, which mathematically amounts to the equality between their modal propagation constants (effective refractive indices). Over the past decade, driven by the need for miniaturization of SPR sensors, various compact configurations enabling coupling between optical waveguide modes and surface plasmonic waves have been investigated. Among others, metallized single mode, multimode and polarization maintaining waveguides and fibers, metallized tapered fibers, metallized fiber Bragg gratings [2, 3, 9, 12, 17, 21, 25, 26, 40, 41, 43, 56, 58–60, 64] and, recently, solid-core microstructured fibers [19, 24, 35], as well as planar photonic crystal waveguides [51, 52] have been studied. In the majority of

fiber implementations (with an exception of microstructured fibers), one typically strips the fiber polymer jacket and polishes off fiber cladding until the fiber core is exposed; then, a metal layer is deposited directly onto a fiber core. Thus, the functionalized surface of a fiber core is then exposed to an analyte.

Ideally, one would use a single mode fiber or waveguide with all the power traveling in a single Gaussian-like core mode operating near the point of resonant excitation of the plasmon [13, 23, 27, 36, 48, 63]. Gaussian shape of a core mode is important as it is best suited for the excitation by standard Gaussian laser sources. Near the point of phase-matching, most of the energy launched into a waveguide core mode should be efficiently transferred into a plasmon mode. However, in the total internal reflection (TIR) single mode waveguides with low refractive index-contrast, coupling with a plasmon is realized at essentially grazing angles of modal incidence on the metal layer. As follows from the basic SPR theory, coupling at such grazing incidence angles leads to an inevitable decrease of sensitivity of the SPR method. In principle, high index-contrast single mode waveguides (see Fig. 4a) could be employed to increase the angle of modal incidence on the interface. Overall, in the single mode waveguide-based sensors, phase-matching between plasmon and fundamental waveguide mode is typically hard to realize. This is related to the fact that the effective refractive index of a core-guided mode is close to the refractive index of the core material, which is typically larger than 1.45

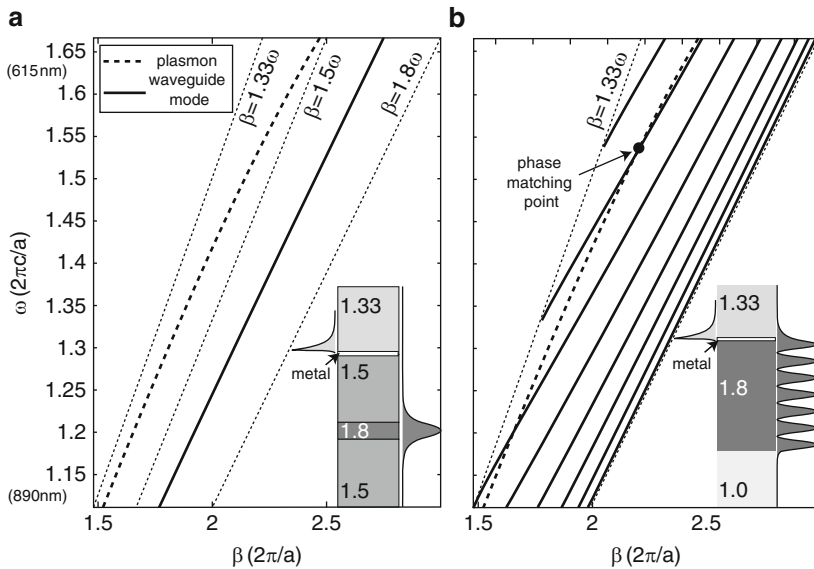


Fig. 4 Band diagrams and schematics of various SPR-based integrated sensor implementations. (a) Single mode waveguide-based sensor. Dispersion relations of a core-guided mode (*solid*) and a plasmon (*thick dashed*). *Inset* – sensor schematic; $|H_{||}|^2$ of a plasmon (*left*) and a core mode (*right*). (b) Multimode waveguide-based sensor. Dispersion relations of the core modes (*solid*) and a plasmon (*thick dashed*). *Inset* – coupler schematic; $|H_{||}|^2$ of a plasmon (*left*) and a high-order mode (*right*) at the phase-matching point (*black circle*)

due to practical material limitations. The effective refractive index of a plasmon is close to the refractive index of an ambient medium, which is typically air $n_a = 1$ (gas sensing) or water $n_a = 1.33$ (biological sensing). Thus, large discrepancy in the effective indices makes phase-matching between the two modes hard to achieve, with an exception of the high frequencies where $\lambda < 650$ nm, where the plasmon dispersion relation deviates towards higher refractive indices. Thus, due to practical limitation on the lowest value of the waveguide core and cladding refractive indices, single mode TIR waveguide-based sensors were demonstrated almost exclusively in the visible region, where phase-matching condition is easier to enforce.

Problems with phase-matching and loss of sensitivity due to shallow angles of incidence could be, in principle, alleviated by using multimode waveguides [10, 17, 21, 58, 64] as presented in Fig. 4b. If launched properly, modal effective propagation angles in such waveguides can be much steeper, also resulting in smaller effective refractive indices. However, in multimode waveguides, only a certain number of higher order modes will be phase-matched with a plasmon. Thus, sensitivity and stability of such sensors depend crucially on launch conditions. Moreover, as spatial field distribution in a Gaussian-like laser source is typically not well matched with the field distribution of a higher order mode of a multimode waveguide, only a small fraction of energy can be launched into such a mode resulting, again, in decreased sensitivity.

In what follows, I detail design principles of a PCF and waveguide-based SPR sensors, and show that they integrate advantages of both the single mode and multimode waveguide-based SPR sensors. Moreover, in PCF and waveguide-based SPR sensors, fundamental Gaussian-like leaky core modes can be phase-matched with a plasmon at any desired wavelength of operation, thus enabling sensing anywhere from the visible to mid-IR. The term “leaky mode” generally refers to the guidance mechanism where the effective refractive index of a propagating mode is smaller than that of the waveguide cladding. Such unusual modes are called leaky modes as, outside of a waveguide core, they do not exhibit a traditional evanescent decay into the cladding, but rather they radiate slowly (leak) into the cladding. Unlike in the case of common TIR waveguides, leaky modes in photonic crystal waveguides are confined by the bandgap of a photonic crystal reflector. As a consequence, the effective refractive index of the fundamental (lowest loss) leaky-core mode can be designed to be arbitrarily smaller than that of a waveguide-core material, thus enabling phase-matching with a plasmon at any desired frequency. Moreover, the lowest loss leaky-core mode typically exhibits a Gaussian-like intensity distribution in the waveguide-core region, thus enabling convenient excitation by a Gaussian beam of an external light source. Using the fundamental (lowest loss) leaky mode for sensing gives the additional advantage of an effectively single mode propagation regime. In particular, when a set of modes is excited at a sensor input, higher-order leaky modes radiate out faster than a fundamental mode. Consequently, after a certain propagation distance, only the fundamental mode is left in the waveguide core. Finally, the effective angle of modal incidence onto a metal film, and hence sensitivity, can be varied by a proper selection of the waveguide core and reflector materials.

4.1 SPR Sensors Using Planar Photonic Bandgap Waveguides

To demonstrate the principles of operation of photonic bandgap waveguide-based SPR sensors, I start by considering plasmon excitation by a Gaussian-like TM polarized mode of a planar photonic crystal waveguide (see Fig. 5a), in which light confinement in a lower refractive index core is achieved by a surrounding multi-layer reflector. TM polarization of the electromagnetic field in a planar multilayer assumes a single magnetic field component $|H_{\parallel}|^2$ directed parallel to the plane of a multilayer, while the electric field component is confined to a plane perpendicular to the multilayer.

The photonic crystal waveguide under consideration consists of 27 alternating layers having refractive indices $n_h = 2.0$, and $n_l = 1.5$. The core layer is layer number 12; having refractive index $n_c = n_l$. Analyte (first cladding) is water $n_a = 1.332$ bordering a 50 nm layer of gold. The substrate refractive index is 1.5. Theory of planar photonic crystal waveguides with infinite reflectors where $n_c = n_l$ [50], predicts that, for a design wavelength λ_c , the effective refractive index $n_{\text{eff}}(\lambda_c)$ of the fundamental TE and TM core-guided modes can be designed, as long as $0 < n_{\text{eff}} < n_l$, by choosing the reflector layer thicknesses as

$$d_{l,h} = \frac{\lambda_c}{4\sqrt{n_{l,h}^2 - n_{\text{eff}}^2}} \quad (15)$$

and by choosing the core layer thickness as $d_c = 2d_l$. Moreover, for this choice of n_c , the field distribution in the core is always Gaussian-like for TE polarized modes, while for TM polarized modes it is Gaussian-like as long as $n_{\text{eff}}^2 > \epsilon_l \epsilon_h / (\epsilon_l + \epsilon_h)$ [50]. By choosing the effective refractive index of a core mode to be that of a plasmon, a desired phase-matching condition is achieved. For a waveguide with a finite reflector, the same design principle holds approximately. Thus, for an operating wavelength of $\lambda = 640$ nm, considered in this example, phase-matching is achieved when the photonic crystal waveguide is designed using $\lambda_c = 635$ nm and $\text{Re}(n_{\text{eff}}(\lambda_c)) = 1.46$ in (15). A reasonable approximation to the $n_{\text{eff}}(\lambda_c)$ is a value of the effective refractive index of a plasmonic wave propagating at a planar gold–analyte interface:

$$n_{\text{eff}}(\lambda_c) = \left(\frac{\epsilon_{\text{gold}}(\lambda_c) \times \epsilon_a(\lambda_c)}{\epsilon_{\text{gold}}(\lambda_c) + \epsilon_a(\lambda_c)} \right)^{1/2}, \quad (16)$$

where ϵ_a is the dielectric constant of an analyte and ϵ_{gold} is the dielectric constant of the gold layer approximated by the Drude model:

$$\epsilon_{\text{gold}}(\lambda_c) = \epsilon_{\infty} - \frac{(\lambda/\lambda_p)^2}{1 + i(\lambda/\lambda_t)}, \quad (17)$$

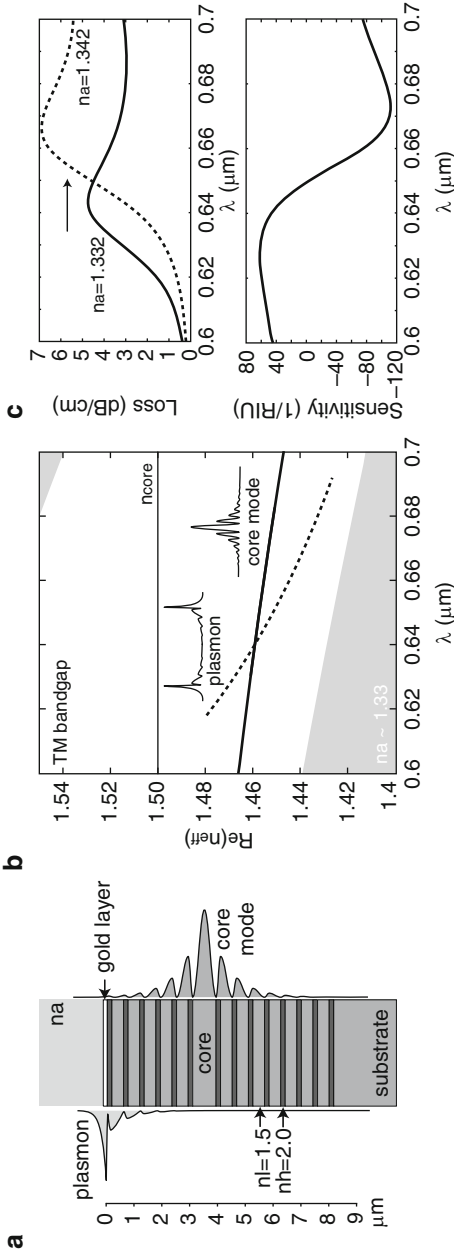


Fig. 5 Planar photonic bandgap waveguide-based SPR sensor. (a) Schematic of a sensor. Low refractive index core is surrounded by the periodic photonic crystal reflector. Top side of the reflector is goldplated for plasmon excitation. Gold layer is bordered by aqueous analyte. $|H_{\parallel}|^2$ field distribution in the fundamental core mode is shown on the *right*, while field distribution in a plasmon mode is shown on the *left* of a sensor schematic. (b) Band diagram of sensor modes. Dispersion relation and field distribution of the fundamental core mode (*thick solid curve*), and plasmon mode (*dashed curve*). TM bandgap of a periodic reflector is shown as a clear region, while *gray* regions correspond to the continuum of the bulk reflector states. By design, the effective refractive index of a core-guided mode can be made significantly smaller than that of the waveguide core material. (c) *Upper part*: *solid curve* shows loss of a waveguide core mode near the phase-matching point with a plasmon at which modal loss peaks. *Dashed line* shows shift of the modal loss curve when refractive index of the analyte is varied. *Lower part*: dependence of the sensor amplitude sensitivity on wavelength

where the choice $\varepsilon_\infty = 9.75$, $\lambda_t = 13 \mu\text{m}$, $\lambda_p = 0.138 \mu\text{m}$ presents one of the many possible fits of the experimental data.

In Fig. 5b, I present band diagram of a planar photonic crystal waveguide-based SPR sensor. All the simulations are performed using standard transfer matrix theory on a complete system that includes both the waveguide and metal layer. Gray regions signify bulk states of a periodic reflector. The clear region in Fig. 5b is a TM bandgap where no extended into the reflector states are found. The thick solid line, which is almost parallel to the band gap edges, marked as “core mode” is a dispersion relation of a Gaussian-like leaky core mode with most of its modal energy concentrated in the low refractive index core. The dashed line marked as “plasmon” represents the dispersion relation of a plasmon mode. Most of the plasmon energy is concentrated at the metal/analyte interface.

Near the phase-matching point, fields of a core-guided mode contain strong plasmonic contribution. As plasmon wave exhibits very high propagation loss, the loss of a core mode (upper plot in Fig. 5c) will also exhibit a sharp increase near the phase-matching point with a plasmon. An important aspect of the proposed setup is the freedom of adjusting the loss of a core mode. As leaky mode decays exponentially fast with respect to distance into the multilayer reflector, coupling strength between the plasmon and core modes can be controlled by changing the number of reflector layers situated between the waveguide core and a metal film. Ultimately, higher coupling strength leads to higher modal losses, hence, shorter sensor length. When the real part of the analyte’s refractive index is varied, the plasmon dispersion relation displaces accordingly, thus leading to a shift in the position of the phase-matching point with a core-guided mode. Consequently, in the vicinity of the phase-matching point, transmission loss of a core-guided mode varies strongly with changes in the analyte’s refractive index; see the upper part of Fig. 5c.

I would like to point out that what is identified as a “core mode” in all the figures in this chapter is in fact a waveguide supermode that includes both the core-guided mode and plasmonic contribution. Since the plasmon mode is extremely lossy, only a small mixing of this mode with the core mode is necessary to achieve sensing. I found pertinent to also show on the graphs what a plasmon mode looks like near the phase-matching point, although this mode by itself is not used in the sensing arrangements. Depending on the designs, the plasmon contribution to the evanescent tail of a core mode is not always visible on the field distribution plots as only the real components of the modes are truly phase-matched.

The simplest mode of operation of a waveguide-based SPR sensor is detection of small changes in the bulk refractive index of an analyte. Similarly to the case of hollow-core PBG fiber-based sensors, there are two main modalities of SPR detection: amplitude-based and spectral-based. In both methodologies, sensing is enabled through detection of changes in the location of a sharp plasmonic loss peak, whose spectral position is strongly dependent on the value of the ambient refractive index. In the amplitude-based approach, all the amplitude measurements are performed at a single wavelength near the center of a plasmonic peak. The advantage of this method is its simplicity and low cost, as no spectral manipulation is required. The disadvantage is a smaller dynamic range and lower sensitivity when compared

to the wavelength interrogation approach, in which the whole transmission spectra are taken and compared before and after the change in the analyte has occurred. I now use expression (5) to define sensor amplitude sensitivity with respect to changes in the real part of an analyte's refractive index. In (5), the measurand δ is $\text{Re}(\Delta n_a)$, and $\alpha(\delta, \lambda)$ is propagation loss of a core-guided mode presented at the top of Fig. 5c. At the bottom of Fig. 5c, I present amplitude sensitivity of a PBG waveguide-based SPR sensor as a function of the wavelength of operation. Maximal sensitivity is achieved at 673 nm and is equal to 112 RIU^{-1} . It is typically a safe assumption that 1% change in the transmitted intensity can be detected reliably, which leads to a sensor resolution of $9 \times 10^{-5} \text{ RIU}$. In the wavelength interrogation mode, changes in the analyte's refractive index are detected by measuring displacement of a plasmonic peak center wavelength λ_p as a function of the value of an analyte's refractive index. Sensor sensitivity is then defined by expression (7), where $\delta = \text{Re}(\Delta n_a)$. I find that the spectral sensitivity of a PBG waveguide-based sensor is $2,300 \text{ nm RIU}^{-1}$. Assuming that a 0.1 nm change in the position of a resonance peak can be detected reliably, sensor resolution of $4.3 \times 10^{-5} \text{ RIU}$ is obtained.

Finally, sensor length is always in the range $L \sim 1/\alpha(\delta, \lambda)$. In the vicinity of plasmonic peak shown in Fig. 5c, the typical sensor length is $L \sim 1 \text{ cm}$. Detailed simulations also show that, similarly to the case of resonant sensing using hollow-core PBG fibers, sensitivity of a PBG waveguide-based plasmonic sensor is only weakly dependent on the sensor length. Particularly, by varying the number of reflector layers separating the waveguide core and gold layer, one can vary the overall sensor length from sub-millimeters to several centimeters without changing significantly the sensor sensitivity.

In the rest of this section, I present theoretical study of SPR sensor designs based on photonic bandgap fibers, rather than planar waveguides. Advantages of fiber-based sensors over their planar counterparts include lower manufacturing cost, possibility of distributed sensing, and incorporation of microfluidics into the fiber structure directly at the fiber drawing step. In what follows I demonstrate an SPR sensor using solid-core PBG Bragg fiber operating at 760 nm, as well as an SPR sensor using honeycomb lattice photonic bandgap fiber operating at 1,060 nm.

4.2 SPR Sensors Using Photonic Bandgap Bragg Fibers

I start by describing solid-core Bragg fiber-based SPR sensor for detection in aqueous analytes. In such a sensor, a thin gold layer is deposited on the outer surface of a Bragg fiber in direct contact with an analyte. By tailoring the dispersion relation of the core-guided mode of a Bragg fiber, phase-matching with a plasmon wave can be obtained at any wavelength in the visible and near-IR. The mode of operation in such a sensor is a Gaussian-like HE_{11} core mode. Effective refractive index of such a mode is matched with that of a plasmon by the proper choice of the

fiber core size. The choice of an HE_{11} mode over the other modes is motivated by the ease of its excitation using common Gaussian laser sources.

As an example, I consider solid-core photonic crystal Bragg fibers made of two materials with refractive indices $n_l = 1.42$ and $n_h = 1.6$. Prototypes of such fibers have been recently fabricated in our group by using a poly(vinylene difluoride) (PVDF)/polycarbonate (PC) material combination [18]. In such fibers, a solid core of refractive index n_l is surrounded by N alternating high and low refractive index reflector layers of thicknesses d_l and d_h (see Fig. 6a). In a manner similar to the planar multilayer waveguides, reflector layer thicknesses are given by the quarter-wave condition (15), where λ_c is an operating wavelength, and $n_{\text{eff}}(\lambda_c)$ is a desired effective refractive index of a core-guided mode at that wavelength. Although such a choice of the reflector parameters guarantees bandgap guidance at λ_c of a mode with effective refractive index $n_{\text{eff}}(\lambda_c)$; however, it does not guarantee existence of such a mode. One way of positioning a core mode dispersion relation inside of the reflector bandgap is by varying the fiber-core diameter d_c , namely, in the large-core diameter Bragg fibers with $d_c \gg \lambda_c$, effective refractive index of the fundamental core mode is close to that of the core material. By decreasing the fiber core size, one can consistently reduce the core mode effective refractive index, and, eventually, position it in the middle of the reflector bandgap. Moreover, in the context of SPR sensing, λ_c also corresponds to the wavelength of phase-matching between plasmon and a core-guided mode. Therefore, a good approximation to $n_{\text{eff}}(\lambda_c)$ of a core-guided mode is that of the effective refractive index of a plasmonic wave propagating at a planar gold-analyte interface given by (16). With these choices of $n_{\text{eff}}(\lambda_c)$ and d_c , one parameter still remains undetermined, which is the number of layers N in the Bragg reflector. In metallized Bragg fibers, guided modes incur additional losses due to high absorption in the metal film. When operating within bandgap of a Bragg fiber reflector, the fields of leaky core modes decay exponentially fast into the reflector. Therefore, modal presence in the metal layer also decreases exponentially fast when increasing the number of reflector layers. Thus, the choice of the number of reflector layers primarily affects the core mode propagation loss and, consequently, the sensor length. As mentioned earlier, PBG fiber-based sensor sensitivity is only weakly dependent on sensor length. Therefore, without the loss of sensitivity, one would choose a small enough number of reflector layers, so that the resultant fiber is short enough to prevent the necessity of coiling and simplify sensor handling.

In Fig. 6, I present an example of a solid-core PBG fiber-based SPR sensor. By choosing the fiber core size to be small, one can considerably reduce the effective refractive index of the core mode. This enables plasmonic excitation at longer wavelengths in the near-IR. In Fig. 6a, I show cross section of a small-core Bragg fiber-based sensor, as well as energy flux distributions in the HE_{11} core mode and plasmon mode. Reflector layer thicknesses are chosen according to (15), where $\lambda_c = 760$ nm, $n_l = 1.42$, $n_h = 1.6$, and $n_{\text{eff}} = 1.39$, thus resulting in $d_l = 654$ nm, $d_h = 240$ nm. The fiber-core diameter is $d_c = 1.8$ μm . The total number of layers is $N = 12$. For the fundamental Gaussian-like mode, the amount of energy in the core is 78%. In Fig. 6b, I present the band diagram of the modes of thus defined

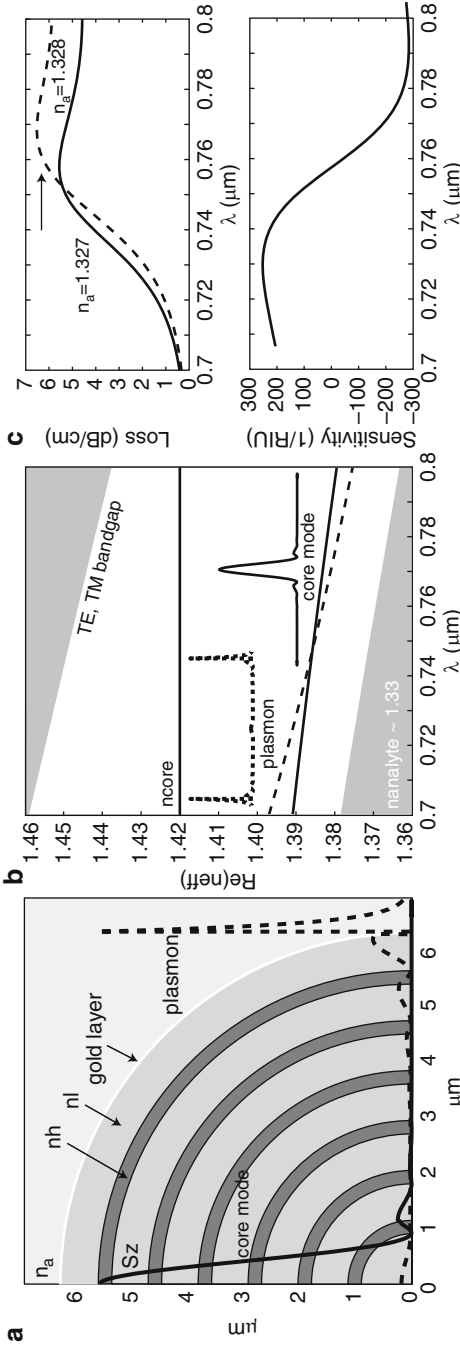


Fig. 6 Small solid-core PBG Bragg fiber-based SPR sensor. (a) Schematic of a sensor. Low refractive index core is surrounded by the concentric photonic crystal reflector. Reflector exterior is goldplated for plasmon excitation. Gold layer is bordered by aqueous analyte. Energy flux distribution across the fiber cross section is shown as a *solid curve* for the fundamental core mode, and as a *dashed curve* for the plasmon mode. (b) Band diagram of the sensor modes. Dispersion relation of the fundamental core mode (*thick solid curve*), and plasmon mode (*dashed curve*), TE, TM bandgap of a periodic planar reflector is shown as a clear region, while *gray* regions correspond to the continuum of bulk reflector states. In a small-core Bragg fiber, effective refractive index of the fundamental core mode can be much smaller than refractive index of the core material. (c) *Upper plot*: solid curve shows loss of the fundamental core mode near the phase-matching point with plasmon. Modal loss reaches its maximum at the phase-matching wavelength. Dashed line corresponds to the shifted modal loss curve when the analyte’s refractive index is varied. *Lower plot*: sensor amplitude sensitivity as a function of wavelength (after [19] © 2007 OSA)

Bragg fiber sensor. The common TM, TE bandgap of a corresponding infinitely periodic Bragg reflector is presented as a clear region, while gray regions define a continuum of reflector bulk states. In a small-core Bragg fiber, the effective refractive index of the core-guided HE_{11} mode (thick solid line) can be considerably smaller than the refractive index of a core material (thin solid line). Dispersion relation of a plasmon mode is shown as thick dashed line. In this particular case, the dispersion relation of the core-guided mode is shifted towards the lower edge of the reflector bandgap; therefore, the core mode (solid curve in Fig. 6a) and plasmon mode (dashed curve in Fig. 6a) penetrate significantly into the reflector. Phase-matching between the core and plasmon modes is achieved at 758 nm. In the upper plot of Fig. 6c, propagation loss of the core-guided mode is presented as a function of the wavelength. As seen from this plot, core mode loss peaks at the wavelength of phase-matching with plasmon mode. In the lower plot of Fig. 6c, I present amplitude sensitivity (5) of a solid-core Bragg fiber-based SPR sensor with respect to changes in the real part of the analyte's refractive index. Maximal sensitivity is achieved at 788 nm and is equal to 239 RIU^{-1} . Assuming that a 1% change in the transmitted intensity can be detected reliably, this leads to a sensor resolution of $3.4 \times 10^{-5} \text{ RIU}$. Finally, I find that the corresponding spectral sensitivity (7) is 10^4 nm RIU^{-1} . Assuming that a 0.1 nm change in the position of a resonance peak can be detected reliably, this leads to a sensor resolution of $9.8 \times 10^{-6} \text{ RIU}$. The sensor length in this case is in a 1 cm range.

4.3 SPR Sensors Using Photonic Bandgap Honeycomb Fibers

In the two previous subsections, I have presented design strategies for the SPR sensors based on photonic crystal Bragg fibers. In principle, any photonic bandgap fiber can be used in place of a Bragg fiber to develop such sensors. In this section, I present an example of a SPR sensor based on a solid-core honeycomb PCF.

In Fig. 7a, schematic representation of a honeycomb PCF-based SPR sensor is presented. The design parameters are chosen as follows: the center to center distance between adjacent holes is $\Lambda = 0.77 \mu\text{m}$, the cladding hole diameter is $d = 0.55\Lambda$ and the diameter of the hole in the core center is $d_c = 0.35\Lambda$. The fiber is made of silica glass with a refractive index of $n_{\text{glass}} = 1.45$, the core and cladding holes are filled with air $n_{\text{air}} = 1$, while the large semicircular channels are plated with a 40 - nm - thick layer of gold and filled with an aqueous analyte $n_a = 1.32$. The central hole in the fiber core lowers its effective refractive index compared to that of a silica cladding. Under certain conditions, such a core can support a mode confined by the bandgap of the honeycomb reflector. The core-guided mode in such a fiber is analogous to that of the small solid-core Bragg fiber discussed earlier. Guided by the bandgap of the fiber reflector, the effective refractive index of the core mode can be made much lower than that of the silica material. Moreover, as in the case of photonic crystal Bragg fibers, radiation loss of a bandgap-guided core

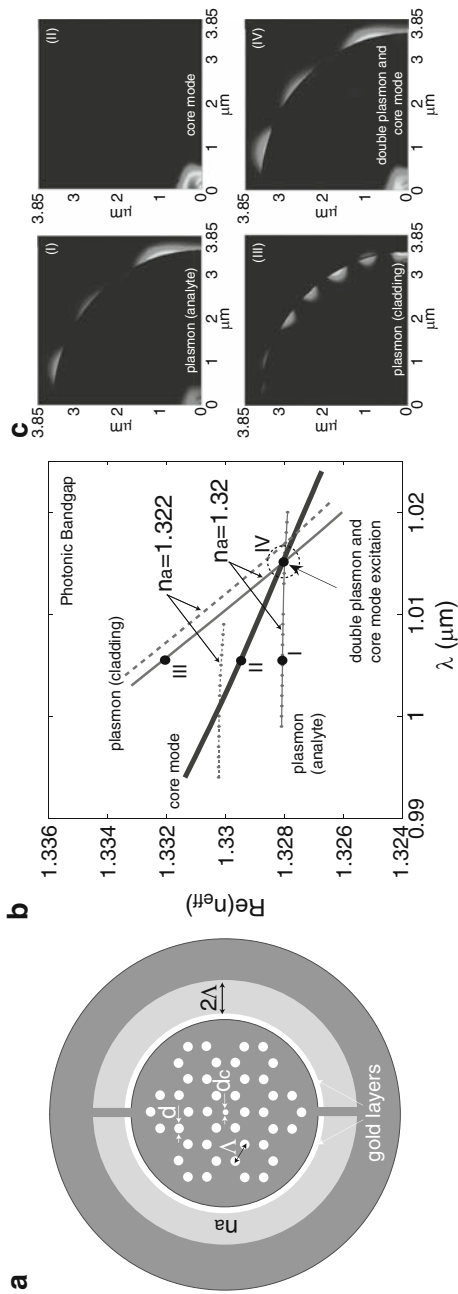


Fig. 7 Solid-core honeycomb photonic crystal fiber-based SPR sensor. (a) Schematic of a sensor. Solid fiber core having a small central hole is surrounded with a honeycomb photonic crystal reflector. Two large channels are integrated to implement analyte access to the fiber reflector region. The channels are goldplated for plasmon excitation. The gold layer is bordered by an aqueous analyte. (b) Band diagram of sensor modes. Dispersion relation of the fundamental core mode (*thick solid curve*), analyte bound plasmon mode (*dashed curve with circles*), and cladding bound plasmon mode (*dashed curve*). The bandgap of an infinitely periodic reflector is shown as a clear region. (c) The energy flux distributions across the fiber cross section are shown for the fundamental core mode (II) as well as the analyte and cladding bound plasmon modes (I,III) outside of the phase-matching region. The energy flux distribution is also shown for the fundamental core mode at the phase-matching point (IV) showing strong mixing of the fundamental core mode with plasmon modes (after [19] © 2007 OSA)

mode can be reduced by adding more layers into the honeycomb reflector. The main reason why I chose a honeycomb structure of the fiber reflector is because it enables a very large photonic bandgap [6, 42], thus simplifying considerably phase-matching of the core-guided and plasmon modes.

Unlike planar metal/dielectric interface that supports a single plasmonic excitation, finite size, microstructured metal layer separating two dielectrics can support multiple plasmon modes [19, 24]. Thus, when tracking losses of a core-guided fiber mode as a function of wavelength, one typically observes several plasmonic peaks corresponding to phase-matching between the core mode and various plasmon modes. Particularly, one of the plasmon modes will have most of its energy concentrated in one of the neighboring dielectrics, while the other plasmonic excitation will have most of its energy concentrated in the other neighboring dielectric. In principle, simultaneous detection of changes in several plasmonic peaks can improve sensor sensitivity; additionally, it gives a natural reference point in the measurements.

In the case of a honeycomb PCF-based sensor, I design the fiber so that two plasmonic peaks are degenerated at 1,009 nm with $n_a = 1.32$. Figure 7b shows the dispersion relations of the Gaussian-like core mode (thick solid line), analyte bound plasmon mode (thin solid line with circles), and cladding bound plasmon mode (thick solid line). These dispersion relations are positioned well inside the bandgap of an infinite honeycomb reflector, which can be confirmed by the plane wave method [6]. Corresponding flux distributions of the core-guided and plasmon modes are presented in Fig. 7c. The core mode loss shows a single plasmonic peak (solid curve in Fig. 8a). When the refractive index of the analyte is varied, this affects the two plasmonic dispersion relations differently. Particularly, the analyte bound plasmon mode is affected much strongly by the changes in the analyte's refractive index than the cladding bound plasmon mode. As a result, degeneracy is lifted, and two closely spaced plasmonic peaks appear in the core mode loss curve (dashed curve in Fig. 8a). For example, a 0.002 change in the analyte's refractive index splits a single plasmonic peak into two peaks separated by 27.5 nm. This permits a novel spectral detection technique, where relative peak separation can be used to characterize changes in the real part of the analyte's refractive index. By defining spectral sensitivity as:

$$S_\lambda = \lim_{\Delta n_a \rightarrow 0} \frac{\lambda_{\text{peak2}}(n_a + \Delta n_a) - \lambda_{\text{peak1}}(n_a + \Delta n_a)}{\Delta n_a}, \quad (18)$$

I find spectral sensitivity of 1.4×10^4 nm RIU⁻¹. It is typically a safe assumption that a 0.1 nm change in the position of a resonance peak can be detected reliably, which results in a sensor resolution of 7.2×10^{-6} RIU, which is, to my knowledge, the highest reported spectral sensitivity of an aqueous fiber-based SPR sensor.

Finally, in Fig. 8b, I present the amplitude sensitivity of the proposed honeycomb PCF-based sensor as defined by (5). The maximal sensitivity is achieved at 1,009 nm and equals to 400 RIU⁻¹. It is typically a safe assumption that a 1% change in the transmitted intensity can be detected reliably, which leads to a sensor

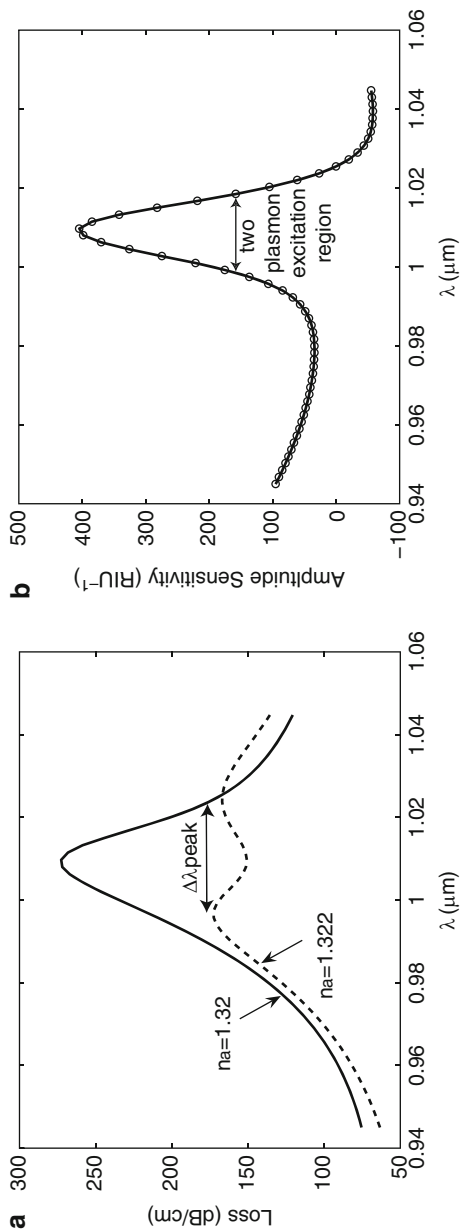


Fig. 8 Sensitivity of the honeycomb photonic crystal fiber-based SPR sensor. (a) The solid curve shows loss of the fundamental core mode near the degenerate phase-matching point with two plasmon modes and $n_a = 1.32$. Due to degeneracy, only one peak is distinguishable in the loss curve. Dashed line shows splitting of the degeneracy in plasmon modes when the analyte's refractive index is changed to $n_a = 1.322$ (b) Dependence of the sensor amplitude sensitivity on wavelength (after [19] © 2007 OSA)

resolution of 2.5×10^{-5} RIU. Note that the sensitivity curve for this sensor design has a single maximum, unlike the sensitivity curves associated with the Bragg fiber designs reported in the preceding section. The sensor length in this case is in 1 mm range.

5 Concluding Remarks

I have described theoretically photonic bandgap (PBG) fiber-based resonant optical sensors of analyte's refractive index. Particularly, I have considered two sensor types. One employed hollow-core photonic bandgap fibers, where core-guided mode is predominantly confined in the analyte-filled core. Another sensor type employed metallized photonic bandgap waveguides and fibers, where core-guided mode was phase-matched with a plasmon wave propagating at the fiber/analyte interface. Both sensor types described in this chapter showed strong resonant dependence of the fiber absorption on the value of the real part of analyte's refractive index, leading to the $10^{-6} - 10^{-4}$ RIU resolution in the real part of the aqueous analyte's refractive index.

References

1. Agranovich VM, Mills DL (1982) Surface polaritons – electromagnetic waves at surfaces and interfaces. North-Holland, Amsterdam
2. Al-Bader SJ, Imaar M (1993) Optical fiber hybrid-surface plasmon polaritons. *J Opt Soc Am B* 10:83–88
3. Alonso R, Subias J, Pelayo J, Villuendas F, Tornos J (1994) Single-mode optical fiber sensors and tunable wavelength filters based on the resonant excitation of metal-clad modes. *Appl Opt* 33:5197–5201
4. Argyros A, van Eijkelenborg MA, Large MCJ, Bassett IM (2006) Hollow-core microstructured polymer optical fiber. *Opt Lett* 31:172–174
5. Balasubramanian S, Sorokulova IB, Vodianov VJ, Simonian AL (2007) Lytic phage as a specific and selective probe for detection of *Staphylococcus aureus* – a surface plasmon resonance study. *Biosens Bioelectron* 22:948–955
6. Barkou SE, Broeng J, Bjarklev A (1999) Silica-air photonic crystal fiber design that permits waveguiding by a true photonic bandgap effect. *Opt Lett* 24:46–49
7. Charlton C, Temelkuran B, Dellemann G, Mizaikoff B (2005) Midinfrared sensors meet nanotechnology Trace gas sensing with quantum cascade lasers inside photonic band-gap hollow waveguides. *Appl Phys Lett* 86:194102
8. Cox FM, Arguros A, Large MCJ (2006) Liquid-filled hollow core microstructured polymer optical fiber. *Opt Express* 14:4135–4140
9. Ctyroky J, Abdelmalek F, Ecke W, Usbeck K (1999a) Modelling of the surface plasmon resonance waveguide sensor with Bragg grating. *Opt Quantum Electron* 31:927–941
10. Ctyroky J, Homola J, Lambeck PV, Musa S, Hoekstra HJWM, Harris RD, Wilkinson JS, Usievich B, Lyndin NM (1999b) Theory and modelling of optical waveguide sensors utilising surface plasmon resonance. *Sensors Actuators B Chem* 54:66–73

11. DeMarco DV, Lim DV (2001) Direct detection of *Escherichia coli* O157:H7 in unpasteurized apple juice with an evanescent wave sensor. *J Rapid Meth Automation Micro* 9:241–257
12. Diez A, Andres MV, Cruz JL (2001) In-line fiber-optic sensors based on the excitation of surface plasma modes in metal-coated tapered fibers. *Sensors Actuators B Chem* 73:95–99
13. Dostalek J, Ctyroky J, Homola J, Brynda E, Skalsky M, Nekvindova P, Spirkova J, Skvor J, Schrofel J (2001) Surface plasmon resonance biosensor based on integrated optical waveguide. *Sensors Actuators B Chem* 76:8–12
14. Fini JM (2004) Microstructure fibres for sensing in gases and liquids. *Meas Sci Technol* 15:1120–1128
15. Jensen JB, Hoiby PE, Emiliyanov G, Bang O, Pedersen LH, Bjarklev A (2005) Selective detection of antibodies in polymer microstructured optical fibers. *Opt Express* 13:5883–5889
16. Johnson SG, Ibanescu M, Skorobogatiy M, Weisberg O, Engeness TD, Soljacic M, Jacobs SA, Joannopoulos JD, Fink Y (2001) Low-loss asymptotically single-mode propagation in large core omniguided fibers. *Opt Express* 9:748–779
17. Jorgenson RC, Yee SS (1993) A fiber-optic chemical sensor based on surface plasmon resonance. *Sensors Actuators B Chem* 12:213–220
18. Gao Y, Guo N, Gauvreau B, Rajabian M, Skorobogata O, Pone E, Zabeida O, Martinu L, Dubois C, Skorobogatiy M (2006) Consecutive solvent evaporation and co-rolling techniques for polymer multilayer hollow fiber preform fabrication. *J Mater Res* 21:2246–2254
19. Gauvreau B, Hassani A, Fehri MF, Kabashin A, Skorobogatiy MA (2007) Photonic bandgap fiber-based Surface Plasmon Resonance sensors. *Opt Express* 15:11413–11426
20. Grigorenko AN, Nikitin P, Kabashin AV (1999) Phase jumps and interferometric surface plasmon resonance imaging. *Appl Phys Lett* 75:3917–3919
21. Gupta BD, Sharma AK (2005) Sensitivity evaluation of a multi-layered surface plasmon resonance-based fiber optic sensor: a theoretical study. *Sensors Actuators B Chem* 107:40–46
22. Harrington JA (2000) A review of IR transmitting hollow waveguides. *Fib Integr Opt* 19:211–227
23. Harris R, Wilkinson JS (1995) Waveguide surface plasmon resonance sensors. *Sensors Actuators B Chem* 29:261–267
24. Hassani A, Skorobogatiy M (2006) Design of the microstructured optical fiber-based surface plasmon resonance sensors with enhanced microfluidics. *Opt Express* 14:11616–11621
25. Homola J (1995) Optical fiber sensor based on surface plasmon resonance excitation. *Sensors Actuators B Chem* 29:401–405
26. Homola J, Slavik R, Ctyroky J (1997a) Interaction between fiber modes and surface plasmon wave spectral properties. *Opt Lett* 22:1403–1405
27. Homola J, Ctyroky J, Skalky M, Hradiliva J, Kolarova P (1997b) A surface plasmon resonance based integrated optical sensor. *Sensors Actuators B Chem* 39:286–296
28. Hoo YL, Jin W, Ho HL, Ju L, Wang DN (2005) Gas diffusion measurement using hollow-core photonic bandgap fiber. *Sensors Actuators B Chem* 105:183–186
29. Kabashin AV, Nikitin P (1998) Surface plasmon resonance interferometer for bio- and chemical-sensors. *Opt Commun* 150:5–8
30. Kim N, Park IS, Kim WY (2007) Salmonella detection with a direct binding optical grating coupler immunosensor. *Sensors Actuators B Chem* 121:606–615
31. Knight JC, Birks TA, Russell RSJ, Rarity JG (1998) Bragg scattering from an obliquely illuminated photonic crystal fiber. *Appl Opt* 37:449–452
32. Konorov SO, Zheltikov AM, Scalora M (2005a) Photonic crystal fiber as a multifunctional optical sensor and sample collector. *Opt Express* 13:3454–3459
33. Konorov SO, Fedotov AB, Zheltikov AM, Miles RB (2005b) Phase-matched four-wave mixing and sensing of water molecules by coherent anti-Stokes Raman scattering in large-core-area hollow photonic-crystal fibers. *J Opt Soc Am B* 22:2049–2053
34. Kretschmann E, Raether H (1968) Radiative decay of non radiative surface plasmons excited by light. *Z Naturforschung A* 23:2135–2142

35. Kuhlmeiy BT, Pathmanandavel K, McPhedran RC (2006) Multipole analysis of photonic crystal fibers with coated inclusions. *Opt Express* 14:10851–10864
36. Lavers CP, Wilkinson JS (1994) A waveguide-coupled surface-plasmon sensor for an aqueous environment. *Sensors Actuators B Chem* 22:475–481
37. Liedberg B, Nylander C, Lundstrom I (1983) Surface plasmon resonance for gas detection and biosensing. *Sensors Actuators B Chem* 4:299–304
38. McLean A (2003) Detection of hydrocarbon fuel spills using a distributed fiber-optic sensor. *Sensors Actuators A Phys* 109:60–67
39. Melendez JL, Carr R, Bartholomew DU, Kukanskis KA, Elkind J, Yee SS, Furlong CE, Woodbury RG (1996) A commercial solution for surface plasmon sensing. *Sensors Actuators B Chem* 35:212–216
40. Monzon-Hernandez D, Villatoro J, Talavera D, Luna-Moreno D (2004) Optical-fiber surface-plasmon resonance sensor with multiple resonance peaks. *Appl Opt* 43:1216–1220
41. Monzon-Hernandez D, Villatoro J (2006) High-resolution refractive index sensing by means of a multiple-peak surface plasmon resonance optical fiber sensor. *Sensors Actuators B Chem* 115:227–231
42. Murao T, Saitoh K, Koshiha M (2006) Design of air-guiding modified honeycomb photonic band-gap fibers for effectively single mode operation. *Opt Express* 14:2404–2412
43. Piliarik M, Homola J, Manikova Z, Ctyroky J (2003) Surface plasmon resonance based on a polarization-maintaining optical fiber. *Sensors Actuators B Chem* 90:236–242
44. Pone E, Dubois C, Dupuis A, Lacroix S, Skorobogatiy M (2006a) Fabrication of the hollow all-polymer Bragg fibers. In: *Proceedings of European Conference on Optical Communication (ECOC)*; We4.4.6, Cannes, France
45. Pone E, Dubois C, Gu N, Gao Y, Dupuis A, Boismenu F, Lacroix S, Skorobogatiy M (2006b) Drawing of the hollow all-polymer Bragg fibers. *Opt Express* 14:5838–5852
46. Russell PSTJ (2006) Photonic crystal fibers. *J Lightwave Technol* 24:4729–4749
47. Shepard JR, Danin-Poleg Y, Kashi Y, Walt DR (2005) Array-based binary analysis for bacterial typing. *Anal Chem* 77:319–326
48. Sheridan AK, Harris RD, Bartlett PN, Wilkinson JS (2004) Phase interrogation of an integrated optical SPR sensor. *Sensors Actuators B Chem* 97:114–121
49. Shi YW, Ito K, Matsuura Y, Miyagi M (2005) Multiwavelength laser light transmission of hollow optical fiber from the visible to the mid-infrared. *Opt Lett* 30:2867–2869
50. Skorobogatiy M (2005) Efficient anti-guiding of TE and TM polarizations in low index core waveguides without the need of omnidirectional reflector. *Opt Lett* 30:2991–2993
51. Skorobogatiy M, Kabashin A (2006a) Plasmon excitation by the Gaussian-like core mode of a photonic crystal waveguide. *Opt Express* 14:8419–8424
52. Skorobogatiy M, Kabashin A (2006b) Photon crystal waveguide-based surface plasmon resonance biosensor. *Appl Phys Lett* 89:211641
53. Smith CM, Venkataraman N, Gallagher MT, Müller D, West JA, Borrelli NF, Allan DC, Koch KW (2003) Low-loss hollow-core silica/air photonic bandgap fibre. *Nature* 424:657–659
54. Smolka S, Barth M, Benson O (2007) Highly efficient fluorescence sensing with hollow core photonic crystal fibers. *Opt Express* 15:12783–12791
55. Snyder AW, Love J (2008) *Optical waveguide theory*, 2nd edn. Springer, London
56. Suzuki H, Sugimoto M, Matsuiand Y, Kondoh J (2006) Fundamental characteristics of a dual-colour fibre optic SPR sensor. *Meas Sci Technol* 17:1547–1552
57. Temelkuran B, Hart SD, Benoit G, Joannopoulos JD, Fink Y (2002) Wavelength-scalable hollow optical fibres with large photonic bandgaps for CO₂ laser transmission. *Nature* 420:650–653
58. Trouillet A, Ronot-Trioli C, Veillas C, Gagnaire H (1996) Chemical sensing by surface plasmon resonance in a multimode optical fibre. *Pure Appl Opt* 5:227–237
59. Tubb AJC, Payne FP, Millington RB, Lowe CR (1997) Single-mode optical fibre surface plasma wave chemical sensor. *Sensors Actuators B Chem* 41:71–79

60. Vidal MB, Lopez R, Alegret S, Alonso-Chamarro J, Garces I, Mateo J (1993) Determination of probable alcohol yield in musts by means of an SPR optical sensor. *Sensors Actuators B Chem* 11:455–459
61. Vienne G, Xu Y, Jakobsen C, Deyerl HJ, Jensen J, Sorensen T, Hansen T, Huang Y, Terrel M, Lee R, Mortensen N, Broeng J, Simonsen H, Bjarklev A, Yariv A (2004) Ultra-large bandwidth hollow-core guiding in all-silica Bragg fibres with nano-supports. *Opt Express* 12:3500–3508
62. Watts H, Lowe C, Pollard-Knight D (1994) Optical biosensor for monitoring microbial cells. *Anal Chem* 66:2465–2470
63. Weiss MN, Srivastava R, Grogner H (1996) Experimental investigation of a surface plasmon-based integrated-optic humidity sensor. *Electron Lett* 32:842–843
64. Weisser M, Menges B, Mittler-Neher S (1999) Refractive index and thickness determination of monolayers by plasmons. *Sensors Actuators B Chem* 56:189–197
65. Zhang LM, Uttamchandani D (1988) Optical chemical sensing employing surface plasmon resonance. *Electron Lett* 23:1469–1470
66. Zourob M, Mohr S, Brown BJT, McDonnell FPR, MB GNJ (2005a) An integrated metal clad leaky waveguide sensor for detection of bacteria. *Anal Chem* 77:232–242
67. Zourob M, Mohr S, Brown BJT, Fielden PR, McDonnell MB, Goddard NJ (2005b) An integrated optical leaky waveguide sensor with electrically induced concentration system for the detection of bacteria. *Lab Chip* 5:1360–1365